


# Sea Surface Imaging Simulation for 3D Interferometric Imaging Radar Altimeter

Zhaoxia Wang , Yongxin Liu, Jie Zhang, and Chenqing Fan

**Abstract**—The interferometric imaging radar altimeter (InIRA) is a new generation radar altimeter, which can provide two-dimensional images of the sea surface topography at high resolution along a wide swath. This article proposes a method for the simulation of sea surface images measured by InIRA. First, the Pierson–Moskowitz wave spectrum and two-scale model are used to simulate the sea surface from which elevation data is to be acquired. This simulated sea surface is then divided into small triangular facets using Delaunay triangulation. Second, the backscattering cross sections of these small facets are calculated via application of quasi-mirror scattering theory, and the backscattering coefficient of the simulated region derived via coherent superposition. Third, system parameters are set, consistent with the basic principle of InIRA. Assuming that the signal transmitted is a linear frequency modulation pulse signal, the simulation images are then derived using the range Doppler and back projection algorithms. By inverting the interferometric phase diagram, elevation estimates can be derived, and compared with original simulated sea levels. This demonstrated accuracy within the centimeter range, verifying the correctness and feasibility of the proposed method.

**Index Terms**—Elevation inversion, interferometric imaging radar altimeter (InIRA), quasi-mirror scattering, sea surface imaging simulation.

## I. INTRODUCTION

OCEAN remote sensing is an important method of marine monitoring and exploration and is a focus of marine science. Sea surface imaging and sea surface topography (SST) are of great importance for oceanographic studies. As an emerging remote sensing information system, interferometric imaging radar altimeter (InIRA) can offer a means to obtain the data of SST with high precision and wide swath [1], [2]. Combining the advantages of traditional radar altimeter with interferometric synthetic aperture radar (InSAR), InIRA eliminates two of the

drawbacks of traditional radar altimeter: small footprints and low spatial resolution. Furthermore, InIRA allows spectral information and elevation data from observed sea surfaces to be collected simultaneously, permitting detection of submesoscale ocean phenomena, and overcomes the limitations hampering sensing in coastal waters by traditional radar altimeters [1]–[5]. InIRA is performed by acquiring two synthetic aperture radar (SAR) complex images of the same region simultaneously since two SAR antennas are borne on satellites [1]. The height value is then recorded by the interferometric phase, which is the phase difference between two SAR complex images. In order to reach the centimeter-level accuracy of height measurement, InIRA system adopts near-nadir incidence, long physical baseline and short radar wavelength. Notably, the near-nadir incidence is the most distinctive characteristic of InIRA from any other existing InSAR systems.

Some countries are currently actively developing InIRA systems. National Aeronautics and Space Administration (NASA) was first to propose such a system named the wide swath ocean altimeter (WSOA) [6]. It was actually a microwave altimeter based on InSAR. It is a pity that WSOA was finally canceled due to some technical limitations at that time [1]. A successor and extension to WSOA, the surface water ocean topography (SWOT) mission [7], [8] was presented by the US National Research Council, and is being jointly developed by the Jet Propulsion Laboratory (NASA/JPL) and the French Center National d'Etudes Spatiales, with release expected in 2020. Its main tasks are as follows. First, mapping mesoscale and submesoscale ocean circulations at a resolution of at least 10 km. Second, estimating the water storage of water bodies exceeding 250 m<sup>2</sup> and rivers over 100 m wide (the target is 50 m) on a global scale, permitting monitoring of changes in this variable at ten-day/monthly/yearly intervals. In China, Zhang *et al.* [4], [5] proposed a new sea-land compatible radar altimeter system in the 1980s, which would also be capable of 3-D imaging, namely the China imaging altimeter (CIALT). The CIALT combined traditional radar altimeter technology, aperture synthesis processing technology, and interferometry technology, giving it both the high precision elevation measurement ability of conventional altimeters and the high-resolution imaging capability of SARs. In 2016, the InIRA system was developed according to CIALT technology and finally applied on TianGong-2 space laboratory. It is reported that this system can measure the sea surface height (SSH) to centimeter-level precision over wide swath, with small incident angle and short baseline interferometry [1], [9]–[10].

Manuscript received April 17, 2020; revised September 17, 2020; accepted October 6, 2020. Date of publication October 26, 2020; date of current version January 6, 2021. This work was supported in part by the China National Key R&D Plan, under Grant 2017YFC1405600, and in part by the Youth Innovation Fund Project at the Marine Telemetry Engineering Technology Research Center of the Ministry of Natural Resources, under Grant 2017002. (Corresponding author: Yongxin Liu.)

Zhaoxia Wang is with the College of Computer Science, Inner Mongolia University, Hohhot 010021, China (e-mail: wangzhaoxia@foxmail.com).

Yongxin Liu is with the College of Electronic Information Engineering, Inner Mongolia University, Hohhot 010021, China (e-mail: yxliu@imu.edu.cn).

Jie Zhang and Chenqing Fan are with the First Institute of Oceanography, Ministry of Natural Resources, Qingdao 266061, China (e-mail: zhangjie@fio.org.cn; fanchenqing@fio.org.cn).

Digital Object Identifier 10.1109/JSTARS.2020.3033164

Numerical simulation provides an effective means to further improve the reliability and accuracy of the InIRA system for SSH measurement. In 2016, Qiu *et al.* [11] and Gaultier *et al.* [12] presented a tool of oceanic field reconstruction that simulates 2-D SSH from the future SWOT mission and analyzed accuracy characteristics of the SWOT data. In 2017, Kong *et al.* [1] simulated the altimeter precision using the system parameters of InIRA on TianGong-2. While there is currently little published literature on imaging simulation for the relatively recent InIRA system, imaging simulation methods for the study of SAR and InSAR have been widely adopted in academia. Wang *et al.* [13] proposed a simulation method for SAR images of the internal waves excited by a submerged object in a stratified ocean, which was used to research the microinternal waves on sea surface in the different radar look directions. Hammer *et al.* [14] used a simulation imaging approach to investigate the SAR signature of oil tanks with fixed and floating roofs. Liu and Chen [15] suggested a method to simulate the SAR images of ship in different motion states by constructing the mesh model of the vessel, and the hydrodynamic models of the dynamic ship wake and ocean surface. Yoshida [16] explained the mechanism of azimuthal ocean wave emerged in SAR image spectra under specific condition based on a numerical simulation. Wang *et al.* [17] proposed a simulation method for oceanic shear-wave-generated eddies, which was employed to research the imaging results of different radar frequencies, look directions of radar, wind speeds, and wind directions. Jung *et al.* [18] simulated the raw data and interferograms of the SuperSAR multiazimuth SAR imaging system, which is used to investigate the feasibility of detecting precise 3-D surfaces. Zhu *et al.* [19] focuses on the study of the raw signal simulation of synthetic aperture radar altimeter (SRAL) for complex terrain surfaces including ice and land surfaces. They analyzed the principle of SRAL, the electromagnetic characteristics of land targets, and the signal processing of SRAL. Sui *et al.* [20] proposed a radar echo tracking model to simulate SSH data obtained by the InSAR altimeter system. Their result shows that the estimated height accuracy for  $1 \times 1$  km and  $2 \times 2$  km resolutions could achieve centimeter-level measurement. These mentioned works give us an impetus for sea surface imaging simulation of InIRA.

In this article, we first use a two-scale model [21], [22] to simulate a sea surface, and then calculate its backscattering coefficient by the physical optics (POs) model and its Kirchhoff approximate solution. Two algorithms are implemented for InIRA sea surface imaging to create simulated images. Finally, we verify the accuracy and feasibility of the proposed method by inverting the SSH from the simulated images. The simulation yields good insight into measurement on a constantly-changing realistic sea surface through the relatively new InIRA system. Depending on the simulation, we can easily analyze and verify the accuracy of SSH measurement at a high resolution along a wide swath. It will be used as a supplementary tool for further optimization of imaging mechanism and improvement on SSH measurement accuracy of the InIRA system.

## II. STOCHASTIC SEA SURFACE SIMULATION

Before imaging the sea surface, we need to simulate the SSH of an area. The process consists of two steps. First, we use a two-scale model to mathematically represent the sea surface. Second, the computed sea surface is divided into small facets in order to subsequently compute backscattering coefficients.

### A. Sea Surface Model

Sea waves are usually composed of wind waves and swells, which are generally considered to be complex and irregular, since they are constantly changing and display clearly random behavior. It is difficult to describe sea waves using deterministic functions and to rapidly measure them with any degree of accuracy. Therefore, to reflect the random features of sea waves, they are often represented as superimpositions of a large number of simple waves with varied amplitudes, frequencies, phases and directions [23].

We adopt a two-scale model to simulate sea surface waves, dividing the sea spectrum into two regions according to different wavelength scales. The short-wave is represented as a Bragg scattering wave generated by a continuous spectrum. The long-wave is represented as a local tangent plane with sinusoidal contours. A simulated random sea surface can be formed as a superposition of the two [24], [25].

A dimensionless 2-D Pierson–Moskowitz (PM) spectrum [26] derived from analysis of observations provides the short-wave spectrum. It has been demonstrated that the PM spectrum provides a good representation of the true sea surface spectrum [27]. The PM direction spectrum can be expressed as

$$S(\omega, \theta) = s(\omega)G(\omega, \theta) \quad (1)$$

where  $s(\omega)$  is the frequency spectrum, and  $G(\omega, \theta)$  is the direction distribution function

$$s(\omega) = \frac{\alpha g^2}{\omega^5} \exp \left[ -\beta \left( \frac{g}{U\omega} \right)^4 \right] \quad (2)$$

where  $\alpha = 8.1 \times 10^{-3}$  and  $\beta = 0.74$ , are dimensionless constants,  $g$  is the gravitational acceleration,  $\omega$  is the angular frequency, and  $U$  is the wind speed at 19.5 m above sea level. The direction distribution function given in (3) is obtained from the stereo wave observation project [28]

$$G(\omega, \theta) = \frac{1}{\pi} (1 + A \cos 2\theta + B \cos 4\theta) \quad (3)$$

$$\begin{cases} A = \left( 0.50 + 0.82 \exp \left[ -\frac{1}{2} \left( \frac{\omega}{\omega_m} \right)^4 \right] \right) \\ B = 0.32 \exp \left[ -\frac{1}{2} \left( \frac{\omega}{\omega_m} \right)^4 \right] \end{cases} \quad (4)$$

where  $\omega_m = 8.565/U$  is the spectral peak frequency. We use a sine wave to simulate the long wave. Let the wavelength be  $\lambda_s$ , and the amplitude  $h_s$ . In 3-D space a sine wave can be expressed

$$z = \frac{h_s}{2} \sin \left( \frac{\pi x}{\lambda_s} \right) \cos \left( \frac{\pi y}{\lambda_s} \right). \quad (5)$$

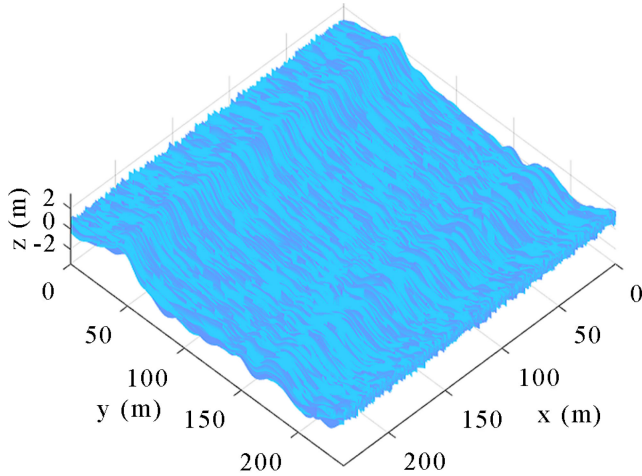


Fig. 1. Simulated random sea surface. This simulated sea surface is  $240 \times 240$  m, with superimposed Gaussian white noise.

### B. Sea Surface Triangulation and Outline Calculation

According to the principles of interaction between electromagnetic waves (Ku band) and the sea surface, the long wave surface is first divided into triangular facets with sizes of similar magnitude to the electromagnetic wavelength. We adopt Delaunay triangulation [29] for this step. Center point coordinates of each facet element are then calculated. The superposition formula given in (6) is used to calculate the sea surface contour [30]

$$z(x, y) = z_0 + k_x(x - x_0) + k_y(y - y_0) + (1 + z_0 k_0)(z_s(x, y) + z_n(x, y)) \quad (6)$$

where  $(x, y, z)$  is the coordinate of a point in a triangular element of sea surface after superposition,  $(x_0, y_0, z_0)$  is the center point coordinate of a triangular facet element on a long wave,  $z_s(x, y)$  is the short-wave amplitude at the point  $(x, y)$ ,  $z_n(x, y)$  is the noise amplitude at the point  $(x, y)$ , and  $k_0$  is the wave number, and  $k_x$  and  $k_y$  are the slopes of the triangle facet in the  $x$  and  $y$  directions, respectively.

In practice, the altitudes of vertices and edges common to surface elements cannot be calculated because different triangular faces on the long wave generally correspond to different values of  $k_x$  and  $k_y$ . Therefore, the value of the superposition at the center point of a triangular element is first obtained via (6), and a sea surface contour then fitted numerically using least squares. An example of the result thus obtained, a complete, continuous, simulated random sea surface, is shown in Fig. 1.

In order to calculate backscattering coefficients for the sea surface, it is necessary to retriangulate sea surface after superposition of long waves and short waves. We divide it into smaller triangular elements with a size similar in magnitude to the incident electromagnetic wavelength. A magnified section after re-triangulation is shown in Fig. 2. Each blue dot is the center of a small triangular facet used for the sampling point in computing the backscattering coefficient and imaging simulation of sea surface.

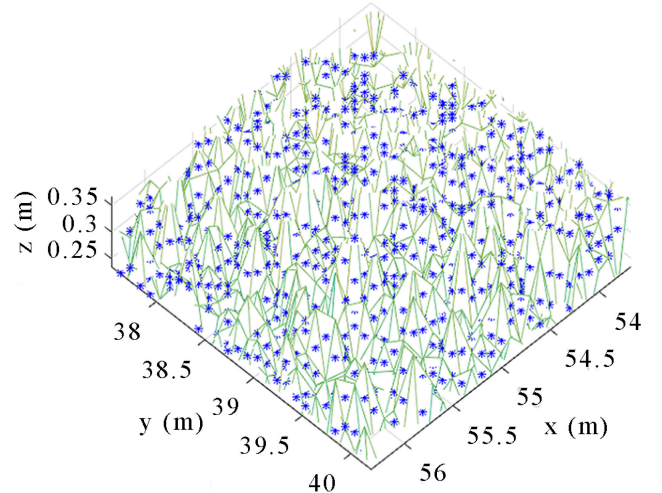


Fig. 2. Rendering of locally enlarged triangulation of sea surface. Blue dots represent center points of triangular elements.

TABLE I  
MAIN SYSTEM PARAMETERS OF THE INIRA USED IN SIMULATION

System Parameter	Value
Carrier frequency	13.75GHz
Platform altitude	393km
Platform angle	$0^\circ$
Incidence angle	$2^\circ - 6^\circ$
Base line	10m
Pulse duration	2.5 $\mu$ s
Chirp bandwidth	300MHz
Sampling frequency	600MHz
Pulse repetition frequency	300Hz

### III. SIMULATION OF SEA SURFACE BACKSCATTERING COEFFICIENT

In the following simulation, InIRA is considered to work at a mode of two antennas. One of them is named main antenna. It is a transceiver which can both transmit and receive signals. The other is slave antenna only receiving signals. The two antennas are imaging the same area of the simulated sea surface. The phases of two obtained images are different due to the different slant ranges between the antennas and target points of sea surface. We use the phase difference, namely interference phase, to calculate SSH values. The parameters of the InIRA system used in the simulation are given in Table I. We adopt the carrier frequency of Ku-band, incidence angle from  $2^\circ$  to  $6^\circ$  and base line of 10 m [1]. Platform altitude is set as 393 km according to [1]. For simplicity, platform angle is assumed to be zero. Other chosen parameters in simulation also meet the general principle of SAR imaging [31], [32].

We also assume a sea surface wave length of 30 m, wind speed of 10 m/s at 19.5 m above the sea level, and average sea surface noise power of  $-20$  db relative to average sea surface echo power of InIRA. The sea surface is subdivided on a triangular grid.

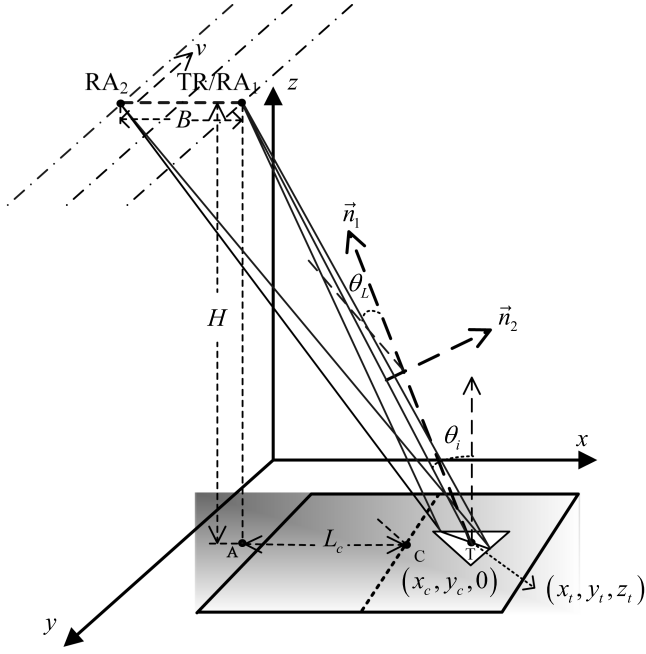


Fig. 3. Interferometric imaging radar altimeter observation geometry. TA/RA1 is an antenna used for both transmitting and receiving, called main antenna. RA2 is another receiving antenna, called slave antenna.  $H$  is the vertical distance between the InIRA radar and sea level.  $v$  is the velocity of radar platform.  $\theta_i$  is the incident angle of the radar electromagnetic wave on the sea level at  $x_t$  in range.  $A$  is the projection of TA/RA1 onto the sea level.  $B$  is the length of the baseline.  $C$  is the center point of the simulated area.  $T$  is the center point of a small facet after triangulation.

The observation geometry of a typical InIRA system is shown in Fig. 3. For ease of calculation it is assumed that the simulated area is completely covered by the InIRA beam, and the central axis of the area on the sea surface irradiated by the beam is assumed to coincide with the central axis of the simulated area in the range direction. Because InIRA adopts the near-nadir looking and height-tracking measurement technique [1]–[10], we assumed that the incident angle of the beam at the central axis is small; the electromagnetic field on the sea surface belongs to the far field of the InIRA radar electromagnetic wave; the electromagnetic wave is planar incident; and the incident angles of all sampling points for the same range time are the same.

Based on these assumptions and using triangulation to simulate facets on a random sea surface, the local angle of incidence  $\theta_L$  for each triangular element can be calculated

$$\theta_L = \left| \frac{\pi}{2} - \arccos \left( \frac{\vec{n}_1 \cdot \vec{n}_2}{|\vec{n}_1| \cdot |\vec{n}_2|} \right) \right|. \quad (7)$$

As shown in Fig. 3,  $\vec{n}_1$  and  $\vec{n}_2$  are normal vectors of, respectively, the triangular facet and the incident plane of the electromagnetic wave.  $\vec{n}_2$  can be derived from  $\theta_i$ , defined as follows:

$$\theta_i = \arctan \left( \frac{L_c - (x_c - x_t)}{H - z_t} \right). \quad (8)$$

As shown in Fig. 3,  $L_c$  is the distance between points  $A$  and  $C$ ,  $x_c$  is the  $x$  coordinate of point  $C$ ,  $x_t$  and  $z_t$  are the  $x$  and  $z$  coordinates of point  $T$ .

Because it is small in size compared to the distance from the sea surface, the InIRA system can be approximated as a moving point. Furthermore, since the transmitter incident angle is small, the incident angle at which the backscattered electromagnetic wave can be received by the antenna must also be very small. Given the electromagnetic scattering characteristics of the sea surface, we use the POs model (i.e., the quasi-mirror scattering model, applicable for an incident angle of less than  $30^\circ$ ) to model the InIRA system's electromagnetic scattering, and calculate its Kirchhoff approximate solution to obtain backscattering coefficients for each small triangular surface element [33], [34]. This can be expressed

$$\sigma_{pq}^0 = \frac{\sec^4 \theta_L}{s^2} \exp \left\{ -\frac{\tan^2 \theta_L}{s^2} \right\} |R_{pq}(0)|^2 \quad (9)$$

$$R_{pq}(0) = R_{hh}(0) = R_{vv}(0) = \frac{1 - \varepsilon}{1 + \varepsilon} \quad (10)$$

where  $R_{pq}(0)$  is the polarization Fresnel reflection coefficient of the surface at normal incidence, the subscript  $h$  represents the horizontal polarization,  $v$  represents the vertical polarization. For sea surfaces whose surface heights follow a Gaussian distribution,  $s^2$  is the surface mean square slope, and  $\varepsilon$  is the relative complex dielectric constant of the targeted sea surface. Assuming a sea surface temperature of  $17.4^\circ\text{C}$ , and salinity of 3.5‰,  $\varepsilon$  can be derived using the Debye formula [35]

$$\varepsilon(S, T, \omega) = \varepsilon_\infty(S, T) + \frac{\varepsilon_1(S, T) - \varepsilon_\infty}{1 + i\omega\tau(S, T)} - \frac{i\sigma(S, T)}{\omega\varepsilon_0} \quad (11)$$

where  $\varepsilon_0 = 8.854 \times 10^{-12}$  is the permittivity of free space,  $\varepsilon_\infty = 4.9$ ,  $\omega$  is the angular frequency of the electromagnetic wave and  $\varepsilon_1$ ,  $\tau$ , and  $\sigma$  are all functions of temperature and salinity.

The backscattering coefficient of each element can be obtained using the above data and formulas. We calculate the radar cross-section of each triangular element as the product of its area (derived using Heron's formula) multiplied by its backscattering coefficient. The sea surface is sampled according to the set range and azimuth sampling unit size ( $2 \times 2$  m). The backscattering coefficient of each sampling point is calculated as the mean value for all triangular elements in the corresponding sampling unit [36]. With  $n$  trihedral elements in a sampling unit, its backscattering coefficient  $\sigma_c$  can be expressed

$$\sigma_c = \frac{\sum_{i=1}^n \sigma_i s_i}{\sum_{i=1}^n s_i}, \quad i = 1, 2, \dots, n \quad (12)$$

where  $\sigma_i$  is the backscattering coefficient of the triangular element and  $s_i$  is its area.

The range-azimuth backscattering coefficient graph is composed of backscattering coefficient values for all sampling points, as shown in Fig. 4(a).

The area of simulated sea surface is  $240 \times 240$  m, and the beam center coincides with the center of this surface. The angle of incidence of the electromagnetic wave on the center of the

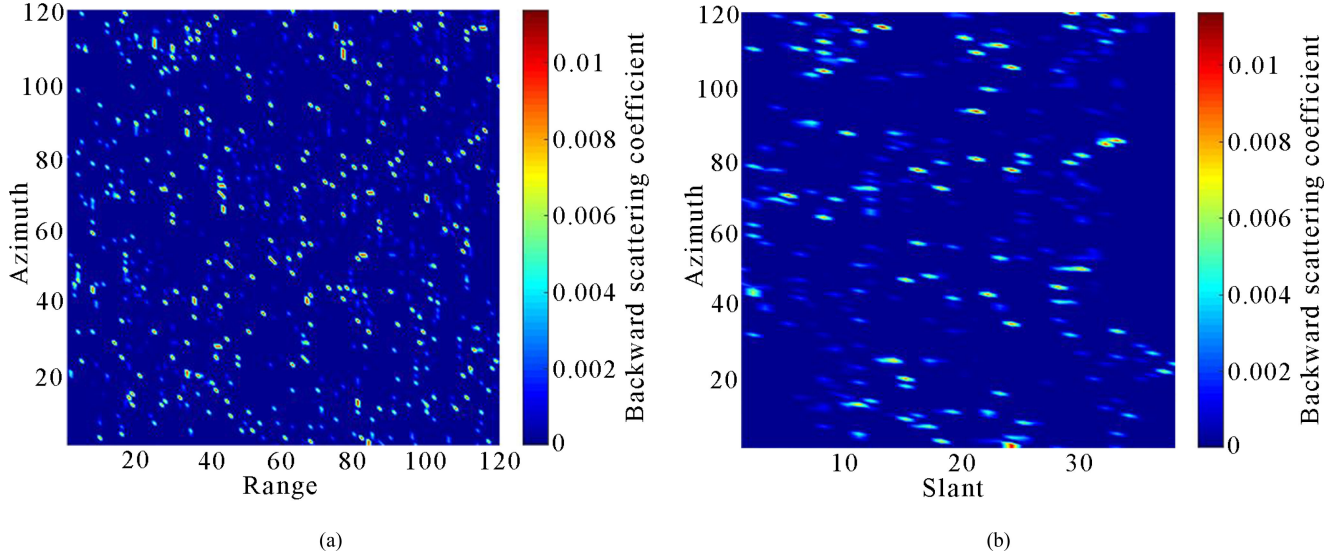


Fig. 4. Sea surface backward scattering coefficient diagram derived using the quasi-mirror scattering model. (a) Range-Azimuth. (b) Slant-Azimuth. Values in color bar represent backward scattering coefficient magnitudes.

simulated region is  $4^\circ$ . Both the resolution of range and azimuth are 2 m.

During imaging, however, the InIRA radar system uses a slant-azimuth coordinate system, so after the interpolation, the range-azimuth backscattering coefficient map must be converted to this system. It is then re-sampled to the slant sampling interval (0.5 m), after which the slant-azimuth backscatter coefficients for the sea surface can be calculated, yielding the slant-azimuth backscatter map shown in Fig. 4(b).

Based on the sea surface backscattering coefficient map thus obtained, two interference complex images for InIRA can be obtained using simulation algorithms [21], [22].

#### IV. SEA SURFACE IMAGING SIMULATION USING THE RANGE DOPPLER (RD) ALGORITHM

##### A. Signal Model

The signal transmitted by the InIRA system can be treated as a linear frequency modulation (LFM) pulse [37]

$$\begin{aligned} s_{tx}(t) &= \text{rect}\left(\frac{t}{T_r}\right) \exp\{2\pi f_0 t + \pi K_r t^2\} \\ &= \omega_r(t) \exp\{2\pi f_0 t + \pi K_r t^2\} \end{aligned} \quad (13)$$

where  $t$  is the quick time (or range time),  $f_0$  is the carrier frequency,  $T_r$  is the LFM pulse duration,  $K_r$  is the range LFM rate. The received signal can be expressed

$$s_{rx}(t, \eta) = \sum_{m=0}^{M-1} A_m w_a(\eta - \eta_c) \cdot B_m + n_m(t, \eta) \quad (14)$$

$$A_m = F_m w_r\left(t - \frac{2R_m(\eta)}{c}\right) \quad (15)$$

$$B_m = \exp\left(-j4\pi \left(\frac{f_0 R_m(\eta)}{c}\right) + j\pi K_r \left(t - \frac{2R_m(\eta)}{c}\right)^2\right) \quad (16)$$

where  $t$  is the quick time (or range time),  $\eta$  is the slow time (or azimuth time),  $2R_m(\eta)/c$  is the time delay,  $R_m(\eta)$  is the distance between target point and radar platform,  $c$  is the velocity of the electromagnetic wave ( $\approx$ speed of light).  $F_m$  is the target reflection attenuation factor, denoting its reflectivity (backscattering coefficient).  $w_a(\eta - \eta_c)$  is the azimuth beam amplitude correction,  $n_m(t, \eta)$  is an additional Gaussian white noise.

##### B. Equivalent Phase Center Processing

For a InIRA system with one transmitting, and two receiving antennas, the path length of the signal received by the main antenna is  $2r_t$  (where  $r_t$  is the oblique distance from the main antenna to the target point), whereas that for the signal received by the slave antenna is  $r_t + r_r$  (where  $r_r$  is the distance from the slave antenna to the target point), rather than  $2r_r$ . At present, the theory underlying all imaging algorithms assumes that the distance from the radar antenna to the target point is  $2r_t$ . Thus, conventional SAR imaging algorithms cannot be applied for InIRA systems with one transmitting, and two receiving antennas. Equivalent phase center processing for the slave antenna must be performed first. In this step, compensation for a fixed phase difference is applied to the slave antenna, after which it is equivalent to a transceiver antenna [38]. Given the measurement geometry of InIRA systems, this transceiver-equivalent antenna is located at the midpoint of the line between the main and slave antennas. Its oblique distance from the target point is  $r_c$ , where  $2r_c = r_t + r_r$ . The phase compensation is given by the following formula:

$$S_{es}(\hat{t}) = S_s(\hat{t}) \exp\left(\frac{j2\pi d}{4r\lambda}\right) \quad (17)$$

where  $S_{es}(\hat{t})$  is the echo signal of the slave antenna after phase compensation,  $S_s(\hat{t})$  is the echo signal received by the slave antenna,  $d$  is the distance from the slave antenna to the main antenna,  $r$  is the distance from the radar antennas' center point to the target plane, and  $\lambda$  is the wavelength of the electromagnetic wave emitted by the InIRA.

### C. RD Algorithm Imaging

The RD algorithm's main process [39], [40] comprises three steps: range compression, range cell migration correction (RCMC), and azimuth compression.

The core method of range compression (or "range matched filtering") involves correlation of a template signal with the radar's echo signal. This is equivalent to performing matched filtering, by convolving the echo signal with a template,  $h(t)$  generated from an inverse time version of the transmitted signal  $s(t)$ . After filtering, a compressed energy pulse centered on the radar reflection delay is generated

$$h(t) = s_{tx}(-t). \quad (18)$$

First, we apply fast Fourier transform (FFT) to  $h(t)$  in (18) and obtain the template signal spectrum. Another FFT is applied to  $s_{rx}(t)$  in (14) to calculate the spectrum of the echo signal. The spectrum of the echo signal is then multiplied by the complex conjugate of the template signal spectrum, yielding the spectrum of the range-compressed signal. Finally, a range-compressed signal was turned into the range-time and azimuth-frequency domains by applying the inverse FFT (IFFT).

The instantaneous oblique distance  $R_m(\eta)$  between the imaging altimeter radar system and the imaging target point undergoes a trend that changes hyperbolically over azimuth time  $\eta$ , leading to range unit migration in the azimuth direction. We assumed the squint angle of InIRA is  $0^\circ$ . Range unit migration with an azimuth frequency of  $f_\eta$  can be calculated in the range-Doppler domain (range-time azimuth-frequency domain) using the following formula

$$R_{rd}(f_\eta) = \frac{R_{om}}{\sqrt{1 - \frac{c^2 f_\eta^2}{4V_r^2 f_o^2}}} \approx \frac{\lambda^2 R_{om} f_\eta^2}{8V_r^2} \quad (19)$$

$$f_\eta \approx -K_a \eta \approx \frac{2V_r^2 \eta}{\lambda R_{om}} \quad (20)$$

where  $R_{om}$  is the minimum instantaneous slant distance,  $V_r$  is the InIRA movement speed,  $K_a$  is the azimuth frequency modulation rate, and  $f_o$  is the carrier frequency.

During the simulation, this migration must be calculated in discrete units. To facilitate correction during the RCMC process, this migration is rounded to the nearest integer.

After RCMC, the echo signal can undergo final processing, namely azimuth compression (or "azimuth matched filtering"). The principles and methods of azimuth compression are basically the same as those for range compression. An azimuth reference signal is necessary, which is similar to the range reference signal, differing only in that the time parameter for the range reference signal is the quick time, while the time parameter for the azimuth reference signal is the slow time.

This is multiplied by the complex conjugate of the echo signal (which has already undergone range compression and RCMC) in the frequency domain and then converted back into the time domain using IFFT, yielding the processed simulated image.

### D. Sidelobe Suppression

However, due to the limited 2-D frequency domain support of InIRA systems, the impulse response function of the receiving device follows a sinc function in both the range and azimuth directions, leading to a high sidelobe level in the simulation image. Local superposition of side lobes seriously affects complex pixel signal values, reducing the accuracy of the postinversion elevation measurements, to the point where their measurement errors exceed centimeter-level tolerances. Thus, these side lobes must be suppressed, and for this we adopt modified spatially variant apodization (MSVA) [41], [42]. The basic idea of MSVA is as follows: the real and imaginary parts of the signal are processed separately, and the value of real (or imaginary) part at a certain point, after sidelobe suppression can be expressed

$$g'(m) = g(m) + Aw_1 + Bw_2 \quad (21)$$

$$A = -2\text{sinc}\left(\left[\frac{f_s}{f_o}\right] w_s\right) g(m) + g\left(m + \left[\frac{f_s}{f_o}\right]\right) + g\left(m - \left[\frac{f_s}{f_o}\right]\right) \quad (22)$$

$$B = -2\text{sinc}\left(2\left[\frac{f_s}{f_o}\right] w_s\right) g(m) + g\left(m + 2\left[\frac{f_s}{f_o}\right]\right) + g\left(m - 2\left[\frac{f_s}{f_o}\right]\right) \quad (23)$$

where  $g(m)$  represents the radar signal before sidelobe suppression,  $g'(m)$  represents the radar signal after sidelobe suppression,  $w_1$  and  $w_2$  are the coefficients of the suppression filter,  $f_s$  represents the sampling rate,  $f_o$  represents the signal bandwidth,  $m$  is the sequence number,  $w_s = f_o/f_s$ , and  $\text{sinc}(m) = \sin(\pi m)/\pi m$ .

In order to avoid invalid inputs, four constraints must be introduced based on normalization requirements and sampling rate center values

$$\left[\text{sinc}\left(\left[\frac{f_s}{f_o}\right] w_s\right) - \cos(\pi w_s)\right] w_1 + \left[\text{sinc}\left(2\left[\frac{f_s}{f_o}\right] w_s\right) - \cos(2\pi w_s)\right] w_2 \leq 0.5 \quad (24)$$

$$[\cos(\pi w_s) - 1] w_1 + [\cos(2\pi w_s) - 1] w_2 \leq 0 \quad (25)$$

$$0 \leq w_1 \leq 1 \quad (26)$$

$$0 \leq w_2 \leq 1. \quad (27)$$

The above representation can be regarded as a linear programming problem, for which maximum and minimum solutions can be found. If the signs of the two solutions differ,  $g'(m) = 0$ . Otherwise,  $g'(m)$  equals the solution with the smaller absolute value. When the algorithm is executed, this method is separately applied to the real and imaginary parts of the RD algorithm's signals output, finally yielding results after sidelobe suppression.

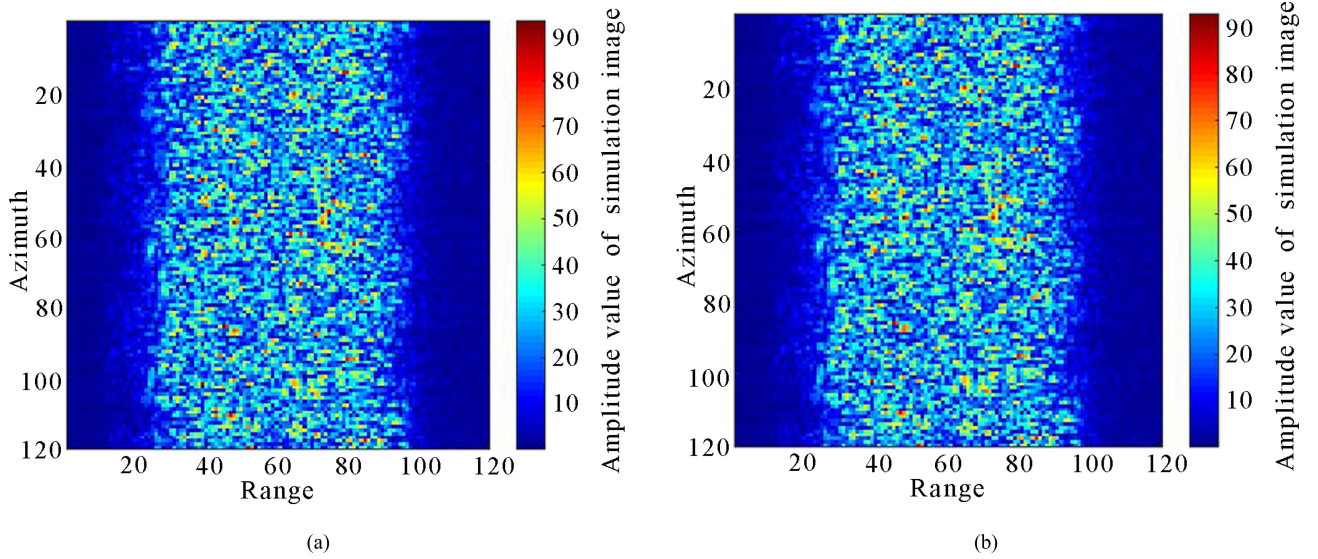


Fig. 5. Amplitude map of InIRA sea surface image simulated using the RD Algorithm. (a) Main antenna. (b) Slave antenna. Values in color bar represent magnitudes of simulated image amplitudes.

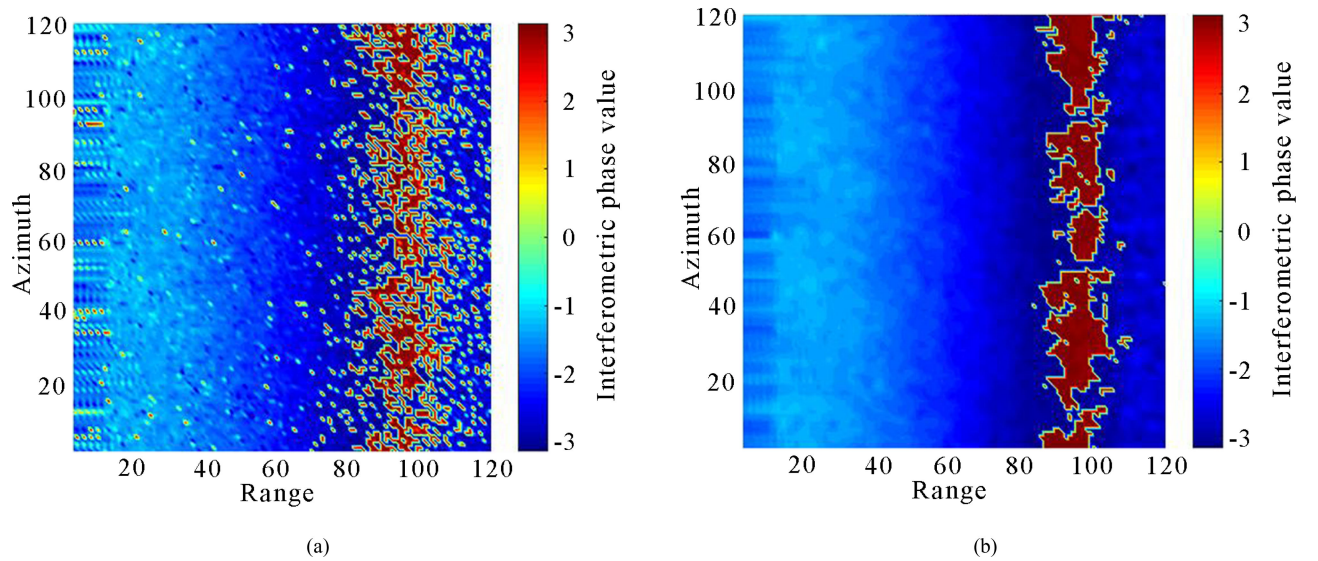


Fig. 6. InIRA interferometric phase diagram simulated using RD Algorithm. (a) Before filtering. (b) After filtering. Values in color bar represent magnitudes of interferometric phase.

Based on the RD imaging algorithm, coherent complex images for two antennas can be simulated, each with a different distance between the receiving antenna and imaging area. We set the simulation time to 1 s. Fig. 5 shows two simulated coherent complex InIRA image magnitude maps for sea surface, on the range-azimuth coordinate system. The complex conjugate of the slave antenna image is multiplied by the main antenna image; the final phase is the interference phase of the two images, as shown in Fig. 6.

There are no light-dark fringes in the interferogram shown in Fig. 6, for the following three reasons.

- 1) The randomness in the distribution of the SSH.
- 2) The relatively low resolution of the InIRA.

- 3) The absence of relative regularity in the phase distribution of the echo sampling points.

#### V. SEA SURFACE IMAGING SIMULATION BASED ON BACK PROJECTION ALGORITHMS

The back projection (BP) algorithm can be directly applied to “range-azimuth” backscatter coefficients, eliminating the need to calculate “slant-azimuth” backscatter coefficients. At the same time, it can be applied in any geometric configuration without imposing any special requirements on the radar platform trajectory. The BP algorithm will also be used to simulate InIRA sea surface images in this article.

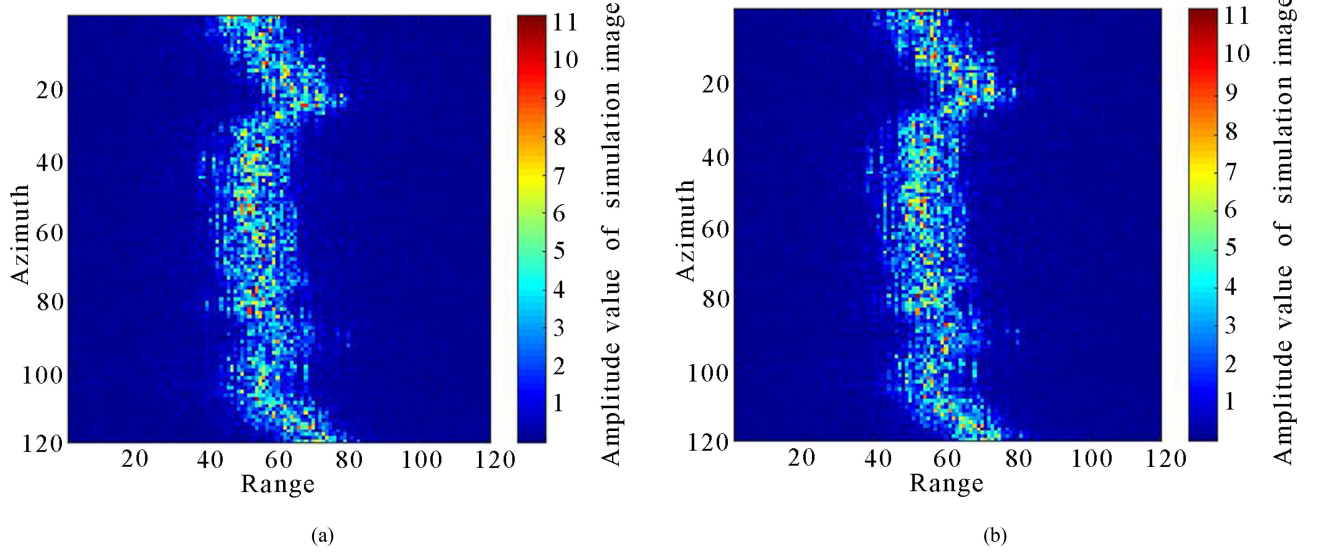


Fig. 7. Amplitude map of InIRA sea surface image simulated using BP algorithm. (a) Main antenna. (b) Slave antenna. Values in color bar represent magnitudes of simulated image amplitudes.

Projecting radar echo data back to each pixel in the imaging region, the BP algorithm image cumulates these pixel values over different azimuth time [43], [44]. An echo signal can be represented

$$s(t, n) = \text{rect}\left(\frac{t-2R_n/c}{T_p}\right) \exp\left(j\pi K_r\left(t-\frac{2R_n}{c}\right)^2\right) \cdot \text{rect}\left(\frac{nV-X_T}{L_s}\right) \exp\left(j2\pi f_c\left(t-\frac{2R_n}{c}\right)\right) \quad (28)$$

where  $c$  is the velocity of the electromagnetic wave,  $T_p$  is the duration of linear frequency modulation pulse,  $K_r$  is the frequency modulation of the linear frequency modulation signal,  $f_c$  is the carrier frequency,  $R_n$  is the distance from the imaging point to the radar platform,  $V$  is the velocity of the platform,  $L_s$  is the length of the synthetic aperture of the InIRA radar,  $X_T$  is the range coordinate of the imaging target point,  $t$  is the slow time, and  $n$  is the fast time.

The sampling point is located at  $(x_i, y_j, z_k)$  after dividing the image area using a grid. The sampling point echo can be expressed

$$s\left(t - \frac{2\sqrt{(x_i - R_x(n))^2 + (y_j - R_y(n))^2 + (z_k - R_z(n))^2}}{c}, n\right) = s(t - t_{ijk}(n), n) \quad (29)$$

where  $R_x(n)$ ,  $R_y(n)$ , and  $R_z(n)$  are the components of  $R_n$  aligned with the  $x$ ,  $y$ , and  $z$  axes, respectively, and  $t_{ijk}(n)$  is the echo signal delay at target point  $(x_i, y_j, z_k)$ . The pixel information  $f(x_i, y_j, z_k)$  for the target point can be obtained by correlating (29) with the actual received scene echo  $s(t, n)$

$$f(x_i, y_j, z_k) = \int_n \int_t s(t, n) s^*(t - t_{ijk}(n), n) dt dn. \quad (30)$$

The equivalent phase center method must also be applied under the BP algorithm to calculate phase compensations for

the slave antenna. The method will not be described here as it is exactly the same as that for the RD algorithm.

(31) describes range compression of the echo signal

$$S_M(t, n) = s(t, n) \otimes s^*(-t, n) = \int_{\tau} s(\tau, n) s^*(\tau - t, n) d\tau. \quad (31)$$

Comparison of (30) and (31) yields the BP algorithm's reconstruction formula

$$f(x_i, y_j, z_k) = \int_n S_M(t_{ijk}, n) dn. \quad (32)$$

In the BP algorithm, for each pixel  $(x_i, y_j, z_k)$  in the imaging region, we can obtain imaging results  $f(x_i, y_j, z_k)$  by coherently superimposing the values of the fast time domain (range direction) matched filtered signals for all azimuth positions  $y(n)$  at time delay  $t_{ijk}(n)$ .

Based on the parameters of the InIRA system given in Table I and the conditions in Section III, two coherent complex InIRA images of the sea surface have been simulated, with amplitude maps as shown in Fig. 7.

Comparing Figs. 5 with 7, we find that the RD and BP algorithms yield significantly different imaging results, and the image intensity from the BP algorithm is significantly smaller than that of images from the RD algorithm. The reason is that part of the energy of the echo signals is lost during discretizing the range compressed echo signals based on the mapping relationship between pixels and geographical space coordinates in azimuth processing of the BP imaging algorithm. It can be also seen that the SST features in azimuth of images acquired by BP imaging algorithm are clearer. This is because the discretization makes the corresponding relationship between the signals on the pixels on simulated images and the real sea surface imaging points more accurate.

The interference phase of the two images, calculated as the phase of the product of the complex conjugate of the slave



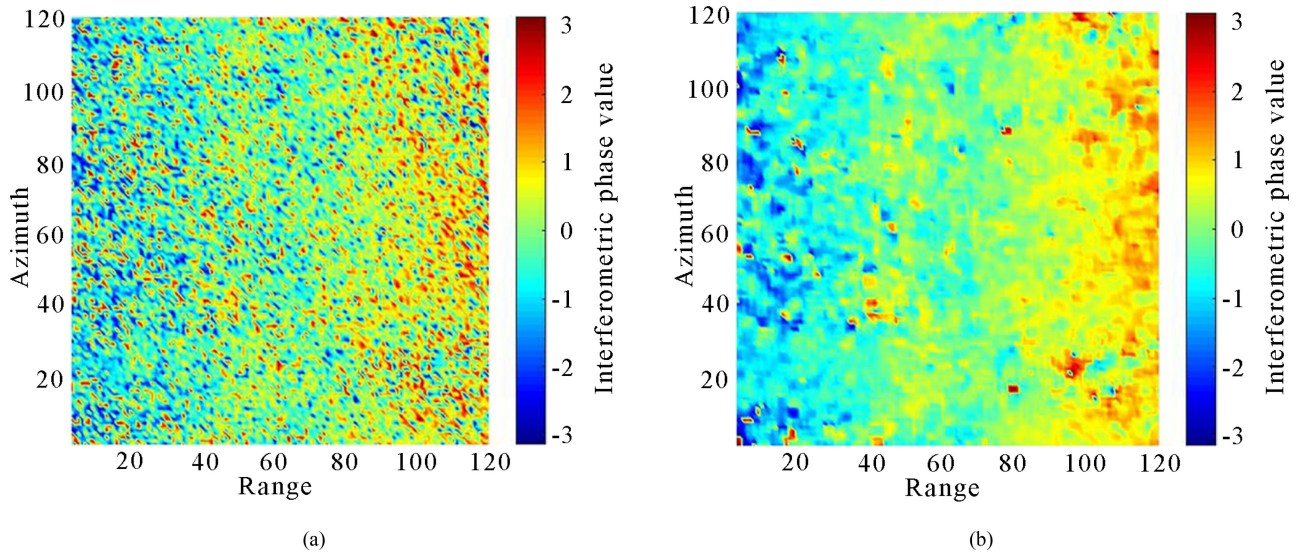


Fig. 8. Simulated interferometric phase diagram of InIRA using BP algorithm. (a) Before filtering. (b) After filtering. Values in color bar represent magnitudes of the interferometric phase.

antenna image and the main antenna image, is shown in Fig. 8(a) and (b). Changes in adjacent phases in the interferograms shown in Fig. 8 are more obvious than in Fig. 6. The phase distribution of Fig. 8 is relatively dispersed, which reflects BP's use of discrete backward projection based on the azimuth time delay during imaging processing. When we adopt the RD algorithm, however, an azimuth time window of one pulse duration is taken as the scale for matched filtering, and the phase distribution of the results has a degree of continuity over the time window.

## VI. VERIFICATION VIA INVERSION

In order to verify the correctness and feasibility of the method, we carried out elevation inversion tests for the main and slave antennas' coherent complex images. According to the principles of interferometry, elevation inversion for simulation InIRA images above involves removing flat earth effect, filtering of interference phases, phase unwrapping and conversing of phase to elevation. Image registration is unnecessary since the two complex images used for inversion represent the same area of sea surface. They are imaged via the main and slave antennas, respectively, and the imaging mechanism and system parameters are the same. Especially, the pixels on the same coordinates of the two images correspond exactly to the target points at the same position on the sea surface.

The main spectral center of the interferometric phase image deviates from zero frequency because of the flat earth effect. In order to extract phase information accurately reflecting SSH, we shifted the main spectral center of the phase map to zero frequency in the frequency domain, in order to eliminate this effect. A cubic spline interpolation is performed to calculate the offset of the main frequency.

As sea surface simulation and imaging results include the influence of random noise (Gaussian white noise), the interferometric phase must be filtered after removing flat earth effect. In

order to maximize the interferogram's edge and detail information, an improved frequency domain filtering method is adopted [45].

After filtering, the interferometric phase of the complex image is the same as that of InSAR, which has a periodic wrapped phase whose values are limited to the range  $(-\pi, \pi]$ .

Referring to the branch tangent phase unwrapping method proposed by Goldstein *et al.* [46], we use the Jonker–Volgenant–Castanon algorithm's [47] notion of minimum global optimal allocation cost to generate branch tangents between positive and negative residual points. By ensuring the balance of branch tangents, their total length is reduced in comparison with the traditional branch tangent method proposed by Goldstein, and the pixel unwrapping rate is improved.

The final step of the inversion process is conversion of the phase value after unwrapping into sea level elevation information. According to the principles of interferometry and assuming an InIRA system with observation geometry of one transmitting, and two receiving antennas, the conversion relationship can be expressed

$$h = H - R_m \cos \left[ \arcsin \left( \frac{\lambda \cdot \phi_{\text{total}}}{4\pi B} \right) \right] \quad (33)$$

$$\phi_{\text{total}} = \phi_u + \phi_r \quad (34)$$

where  $h$  is the height of the target point,  $H$  is the vertical distance from the center of the main antenna to the reference plane (sea level in this article),  $R_m$  is the distance from the main antenna to the target point,  $\lambda$  is the wavelength of the electromagnetic waves emitted by the InIRA,  $B$  is the baseline length,  $\phi_{\text{total}}$  is the absolute phase difference between the signals received by main and slave antennas,  $\phi_u$  is the phase value of after unwrapping, and  $\phi_r$  is the overall phase residual, which, in practice, can be determined using known ground control points [1], [48].

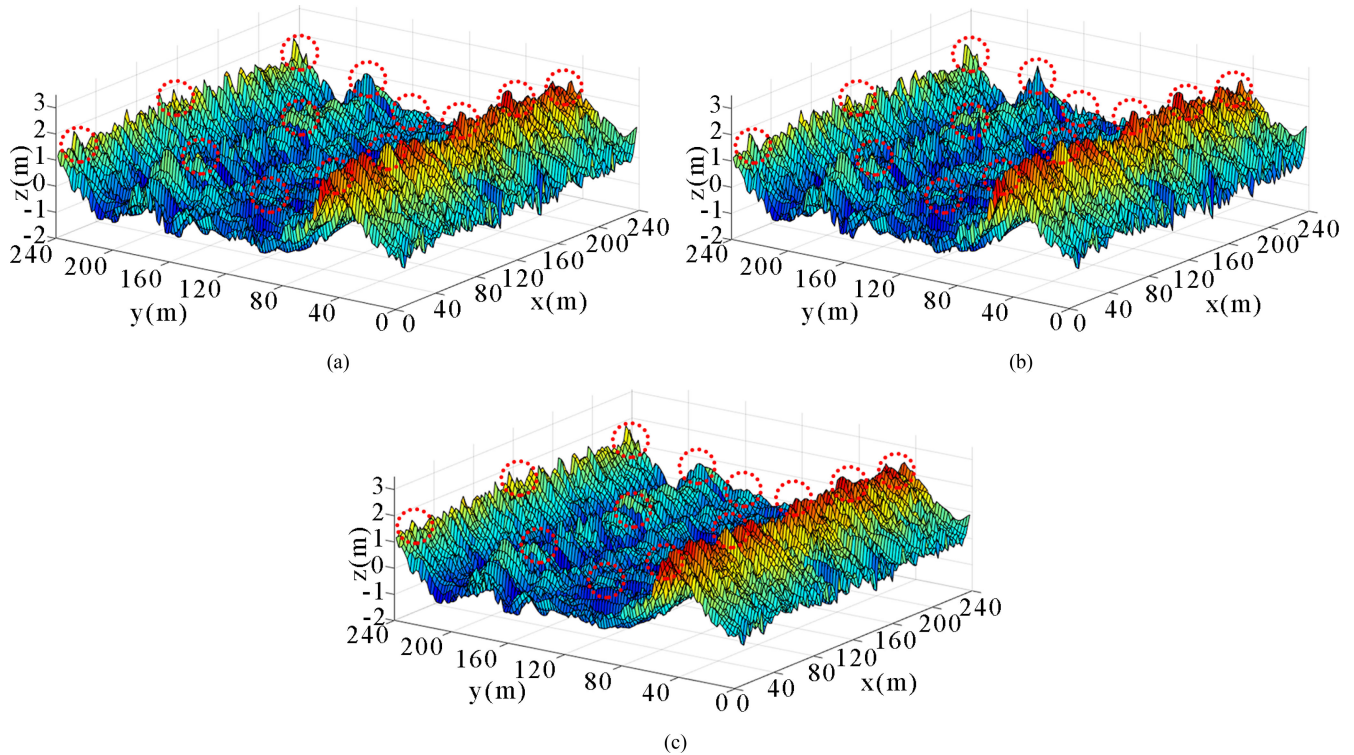


Fig. 9. Elevation map of the sea surface sample point. (a) Simulated sea surface elevation. (b) Inversion sea surface elevation using RD algorithm. (c) Inversion sea surface elevation using BP algorithm. Some relatively obvious visual differences of sea surface elevation have been marked with red circles.

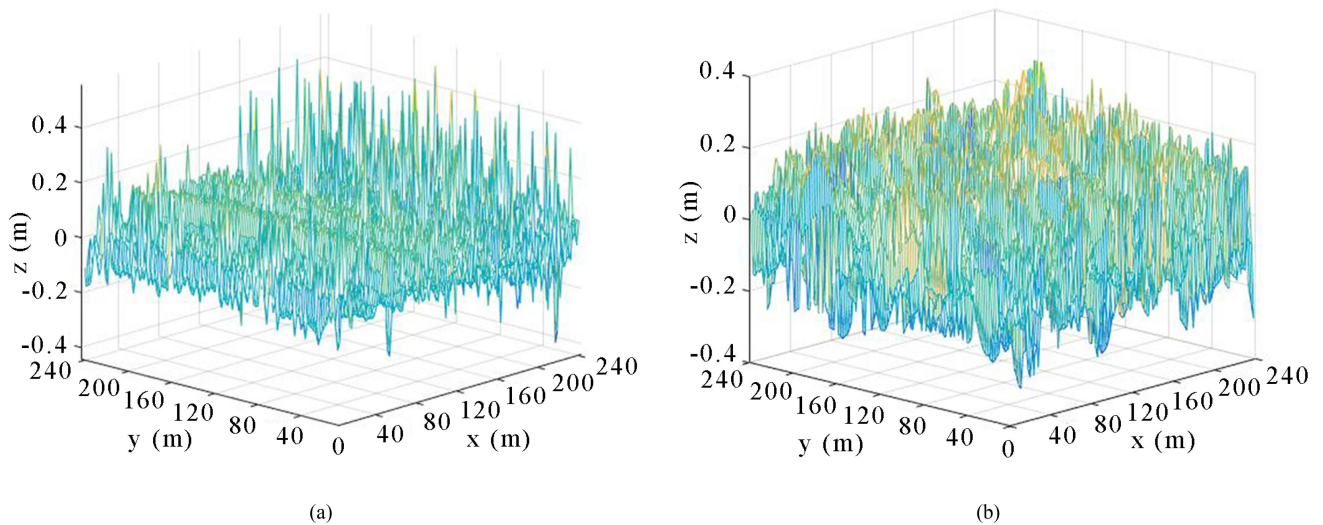


Fig. 10. The error between elevations calculated by inversion and original simulated elevations. (a) Using RD algorithm imaging. (b) Using BP algorithm imaging.

Using the above steps, simulated imaging results derived using the RD and BP algorithms have been inverted; the results shown in Fig. 9(b) and (c).

The elevations derived from the inversion are compared with the original simulated sea level elevations, in the form of errors, shown in Fig. 10(a) and (b). The mean errors are 0.0544 and 0.0851 m, respectively, and the mean square errors are 0.0057 and 0.0114 m, respectively. The error distributions are shown in histogram form in Fig. 11(a) and (b). Figs. 10 and 11 clearly

indicate that the same sea surface target area has been imaged based on the same InIRA system parameters. The inversion elevation errors for the RD algorithm are generally small and hover around 0 m, but elevation errors for some individual positions are large, as the spikes in Fig. 10(a) reveal, along with the errors in the 0.5 m histogram bucket in Fig. 11(a). The SSH errors of the BP algorithm are relatively larger overall, but their distribution is relatively uniform, with no excessively large outliers, and basically no errors in the [0.4, 0.5 m] interval.

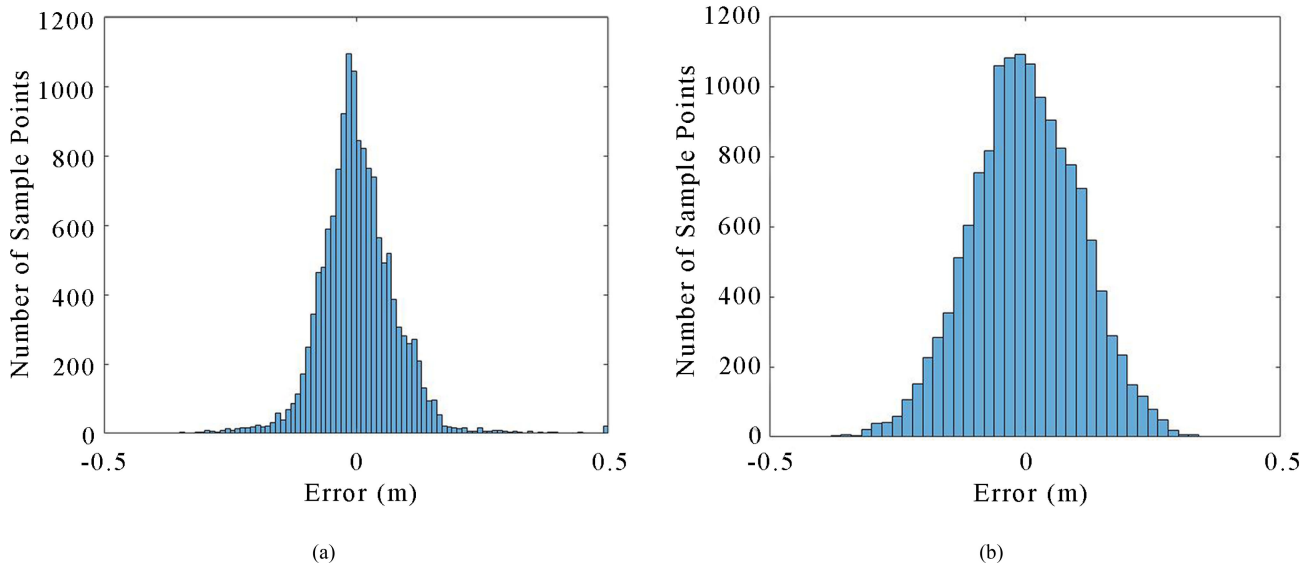


Fig. 11. The histogram of Elevation error distribution. (a) Using RD algorithm imaging. (b) Using BP algorithm imaging.

The main reason for this is that the RD algorithm uses a matched filtering method for azimuth signal processing. The signal within one-time window displays good continuity, and in principle is not subject to matching error. The main source of error is randomness in the sea surface and the InIRA system, with random changes in individual position errors occurring due to differences in the filtering effect. By contrast, the BP algorithm is based on the time delay in azimuth signal processing, and the magnitude of the time delay depends entirely on the instantaneous distance between the target point and the receiving antenna. In 3-D space, this instantaneous distance is not only related to the 2-D sea level coordinates of the sampling point, but also to their height. So, sampling points with the same distance but different positions can sometimes be projected incorrectly, resulting in relatively large overall errors.

## VII. CONCLUSION

In conclusion, we proposed a simulation method of SST imaging for SSH measurement of InIRA. The simulation conforms to the systematic principles of planned SWOT mission and TianGong-2 altimeter. First, the PM wave spectrum and two-scale model were used to simulate a sea surface area from which to obtain elevation data. To permit relatively accurate calculation of backscattering coefficients for this simulated sea surface, it was divided into small triangular facets of dimensions similar to the wavelength of InIRA electromagnetic waves using Delaunay triangulation. Backscattering coefficients were then obtained using a quasi-mirror scattering model and coherence superposition. The RD and BP imaging algorithms were then used to simulate coherent complex InIRA images. Through elevation inversion calculations, the precision of SSH measurement results at sampling points was calculated, and found to fall in the centimeter range at  $2 \times 2$  m resolution, a higher resolution

than that in [20]. The accuracy of SSH measurement will further improve if the resolution value set in the simulation is reduced to that designed in the practical InIRA system.

Based on our simulation approach, an optimized model of error correction and elevation inversion for real InIRA measured SSH images will be further proposed after considering the influence of system parameters and atmospheric perturbation or elevation retrieval performance.

## ACKNOWLEDGMENT

The authors would like to thank the editors and anonymous reviewers for constructive comments which helped improve the presentation of this article.

## REFERENCES

- [1] W. Y. Kong, J. S. Chong, and H. Tan, "Performance analysis of ocean surface topography altimetry by Ku-band near-nadir interferometric SAR," *Remote Sens.*, vol. 9, no. 9, pp. 933, Sep. 2017.
- [2] K. C. Solander, J. T. Reager, and J. S. Famiglietti, "How well will the surface water and ocean topography (SWOT) mission observe global reservoirs," *Water Resour. Res.*, vol. 52, no. 3, pp. 2123–2140, Feb. 2016.
- [3] J. S. Yang, Q. M. Xiao, R. Zhang, H. G. Zhang, and W. G. Huang, "China imaging altimeter and its possible oceanic application," *Proc. SPIE Remote Sens.*, vol. 7473, Sep. 2009, Art. no. 74730U.
- [4] Y. H. Zhang *et al.*, "Design and preliminary experiment of China imaging altimeter," in *Proc. Microw. Remote Sens. Atmos. Environ. III*, Apr. 2003, pp. 190–198.
- [5] Y. H. Zhang, X. K. Zhang, X. Meng, W. Luo, Z. X. Zhou, and J. S. Jiang, "An interferometric imaging altimeter applied for both ocean and land observation," in *Proc. IEEE Int. Geosci. Remote Sens. Symp.*, Jul. 2007, pp. 3821–3824.
- [6] E. Rodriguez, F. Li, C. L. Parsons, and E. Walsh, "Wide swath ocean topography mapping with interferometric altimeters," in *Proc. 12th Can. Symp. Remote Sens. Geosci. Remote Sens. Symp.*, Jul. 1989, pp. 2265–2268.
- [7] B. Qiu, S. M. Chen, P. Kein, C. Uebelmann, L. L. Fu, and H. SasAki, "SWOT sea surface height measurements," *J. Phys. Oceanogr.*, vol. 46, no. 3, pp. 947–963, Mar. 2016.

- [8] I. Turki, B. Laignel, L. Chevalier, S. Costa, and N. Massei, "On the investigation of the sea-level variability in coastal zones using SWOT satellite mission: Example of the eastern English channel (western France)," *IEEE J. Sel. Top. Appl. Earth Observ. Remote Sens.*, vol. 8, no. 4, pp. 1564–1569, Apr. 2015.
- [9] J. S. Yang, L. Ren, and G. Zheng, "The first quantitative ocean remote sensing by using Chinese interferometric imaging radar altimeter onboard TG-2," *Acta Oceanol. Sinica*, vol. 36, no. 2, pp. 122–123, Feb. 2017.
- [10] L. Ren, J. S. Yang, Y. J. Jia, X. Dong, J. Wang, and G. Zheng, "Sea surface wind speed retrieval and validation of the interferometric imaging radar altimeter aboard the Chinese Tiangong-2 space laboratory," *IEEE J. Sel. Top. Appl. Earth Observ. Remote Sens.*, vol. 11, no. 12, pp. 4718–4724, Dec. 2018.
- [11] B. Qiu, S. Chen, P. Klein, C. Ubelmann, L. L. Fu, and H. Sasaki, "Reconstructability of three-dimensional upper-ocean circulation from SWOT sea surface height measurements," *J. Phys. Oceanogr.*, vol. 46, no. 3, pp. 947–963, Sep. 2015.
- [12] L. Gaultier, C. Ubelmann, and L. L. Fu, "The challenge of using future SWOT data for oceanic field reconstruction," *J. Atmos. Ocean. Technol.*, vol. 33, no. 1, pp. 119–126, Nov. 2015.
- [13] L. T. Wang, M. Zhang, and J. K. Wang, "Synthetic aperture radar image simulation of the internal waves excited by a submerged object in a stratified ocean," *Waves Random Complex Media*, vol. 30, no. 1, pp. 1–15, Jul. 2018.
- [14] H. Hammer, S. Kuny, and K. Schulz, "Simulation-based signature analysis of fuel storage tanks in high-resolution SAR images," *IEEE Geosci. Remote Sens. Lett.*, vol. 14, no. 8, pp. 1278–1284, Aug. 2017.
- [15] P. Liu and P. Chen, "Modeling and simulation of vessel in SAR image using oceanographic measured data and shipbuilding drawings," *Int. J. Numer. Model.*, vol. 3, no. 2, Mar. 2020, Art. no. e2673.
- [16] T. Yoshida, "Azimuthal ocean wave emerged in SAR image spectra under specific condition," *J. Geophys. Res.*, vol. 122, no. 12, pp. 9625–9635, Dec. 2017.
- [17] Y. H. Wang, M. Yang, and J. S. Chong, "Simulation and analysis of SAR images of oceanic shear-wave-generated eddies," *Sensors*, vol. 19, no. 7, Mar. 2019, Art. no. 1529.
- [18] H. S. Jung, Z. Lu, A. Shepherd, and T. Wright, "Simulation of the Super-SAR multi-azimuth synthetic aperture radar imaging system for precise measurement of three-dimensional earth surface displacement," *IEEE Trans. Geosci. Remote Sens.*, vol. 53, no. 11, pp. 6196–6206, Jul. 2015.
- [19] Z. Y. Zhu, H. Zhang, and F. Xu, "Raw signal simulation of synthetic aperture radar altimeter over complex terrain surfaces," *Radio Sci.*, vol. 55, no. 2, Feb. 2020, Art. no. e2019RS006948.
- [20] X. H. Sui, R. N. Zhang, F. L. Wu, Y. Li, and X. Y. Wan, "Sea surface height measuring using InSAR altimeter," *Geodesy Geodyn.*, vol. 8, no. 4, pp. 278–284, Mar. 2017.
- [21] J. T. Johnson, R. T. Shin, J. A. Kong, L. Tsang, and K. Pak, "A numerical study of the composite surface model for ocean backscattering," *IEEE Trans. Geosci. Remote Sens.*, vol. 36, no. 1, pp. 72–83, Jan. 1998.
- [22] F. Nunziata, A. Gambardella, and M. Migliaccio, "An educational SAR sea surface waves simulator," *Int. J. Remote Sens.*, vol. 29, no. 11, pp. 3051–3066, May 2008.
- [23] S. C. Wen, "Generalized wind wave spectra and their applications," *Sci. China Ser. A*, vol. 9, no. 3, pp. 377–402, Jan. 1960.
- [24] F. Berizzi and E. D. Mese, "Scattering coefficient evaluation from a two-dimensional sea fractal surface," *IEEE Trans. Geosci. Remote Sens.*, vol. 50, no. 4, pp. 426–434, Apr. 2002.
- [25] F. Berizzi and E. D. Mese, "Scattering from a 2D sea fractal surface: Fractal analysis of the scattered signal," *IEEE Trans. Geosci. Remote Sens.*, vol. 50, no. 7, pp. 912–925, Nov. 2002.
- [26] S. L. Broschat, "Reflection loss from a 'Pierson-Moskowitz' sea surface using the nonlocal small slope approximation," *IEEE Trans. Geosci. Remote Sens.*, vol. 37, no. 1, pp. 632–634, Jan. 1999.
- [27] P. A. Umesh, P. K. Bhaskarana, K. G. Sandhyab, and T. M. Balakrishnan Nairb, "Numerical simulation and preliminary analysis of spectral slope and tail characteristics using nested WAM-SWAN in a shallow water application off Visakhapatnam," *Ocean Eng.*, vol. 173, pp. 268–283, Feb. 2019.
- [28] L. Baer, "An experiment in numerical forecasting of deep-water ocean waves," *J. Geophys. Res.*, vol. 67, no. 9, pp. 3539–3540, Jul. 1962.
- [29] P. O. Persson and G. Strang, "A simple mesh generator in matlab," *SIAM Rev.*, vol. 46, no. 2, pp. 329–345, Jun. 2004.
- [30] G. Franceschetti, A. Iodice, G. Riccio, G. Ruello, and R. Siverio, "SAR raw signal simulation of oil slicks in ocean environments," *IEEE Trans. Geosci. Remote Sens.*, vol. 40, no. 9, pp. 1935–1949, Sep. 2002.
- [31] X. F. Li, H. D. Guo, K. S. Chen, and X. F. Yang, "Introduction to synthetic aperture radar," in *Advances in SAR Remote Sensing of Oceans*, 1st ed., Boca Raton, FL, USA: CRC Press, 2018, pp. 3–19.
- [32] Z. Lu, D. Dzurisin, C. Wicks Jr., and J. Power, "Interferometric synthetic aperture radar (InSAR): A long-term monitoring tool," in *Monitoring Volcanoes in the North Pacific*, 1st ed., Heidelberg, Germany: Springer, 2015, pp. 235–260.
- [33] D. Barrick, "Wind dependence of quasi-specular microwave sea scatter," *IEEE Trans. Antennas Propag.*, vol. 22, no. 1, pp. 135–136, Jan. 1974.
- [34] M. H. Freilich and B. A. Vanhoff, "The relationship between winds, surface roughness, and radar backscatter at low incidence angles from TRMM precipitation radar measurements," *J. Atmos. Ocean Tech.*, vol. 20, no. 4, pp. 549–562, Apr. 2003.
- [35] J. Barthel, K. Bachhuber, R. Buchner, H. Hetzenauer, and M. Kleebauer, "A computer controlled system of transmission lines for the determination of the complex permittivity of lossy liquids between 8.5 and 90GHz," *Berichte Der Bunsengesellschaft Für Physikalische Chemie*, vol. 95, no. 8, pp. 853–859, Aug. 1991.
- [36] J. K. Wang, M. Zhang, J. L. Chen, and Z. H. Cai, "Application of facet scattering model in SAR imaging of sea surface waves with Kelvin wake," *Prog. Electromagn. Res. B*, vol. 67, pp. 107–120, May 2016.
- [37] C. Wang, L. Chen, and L. Liu, "A new analytical model to study the ionospheric effects on VHF/UHF wideband SAR imaging," *IEEE Trans. Geosci. Remote Sens.*, vol. 55, no. 8, pp. 4545–4557, Aug. 2017.
- [38] H. F. Huang and D. N. Liang, "A new effective squint range model of spaceborne bistatic SAR," *Acta Electronica Sinica*, vol. 33, no. 12, pp. 2209–2212, Dec. 2005.
- [39] J. B. Zheng, H. W. Liu, G. S. Liao, T. Su, Z. Liu, and Q. H. Liu, "ISAR imaging of nonuniformly rotating targets based on generalized decoupling technique," *IEEE J. Sel. Top. Appl. Earth Observ. Remote Sens.*, vol. 9, no. 1, pp. 520–532, Jan. 2016.
- [40] K. Aberman and Y. C. Eldar, "Sub-Nyquist SAR via fourier domain range-doppler processing," *IEEE Trans. Geosci. Remote Sens.*, vol. 55, no. 11, pp. 6228–6244, Nov. 2017.
- [41] C. Ni, Y. F. Wang, X. H. Xu, C. Y. Zhou, and P. F. Cui, "A SAR sidelobe suppression algorithm based on modified spatially variant apodization," *Sci. China Tech. Sci.*, vol. 40, no. 12, pp. 1485–1494, Dec. 2010.
- [42] C. R. Carlos, L. R. Sergio, and B. G. Mateo, "Robust SVA method for every sampling rate condition," *IEEE Trans. Aerosp. Electron. Syst.*, vol. 43, no. 2, pp. 571–580, Apr. 2010.
- [43] D. C. Munson, J. D. O'Brien, and W. K. Jenkins, "A tomographic formulation of spotlight-mode synthetic aperture radar," *Proc. IEEE*, vol. 71, no. 8, pp. 917–925, Aug. 1983.
- [44] Z. M. Yang, M. D. Xing, L. Zhang, and B. Zheng, "A coordinate-transform based FFBP algorithm for high-resolution spotlight SAR imaging," *Sci. China Inf. Sci.*, vol. 58, no. 2, pp. 1–11, Feb. 2015.
- [45] Z. Y. Suo, J. Q. Zhang, M. Li, Q. J. Zhang, and F. Chao, "Improved InSAR phase noise filter in frequency domain," *IEEE Trans. Geosci. Remote Sens.*, vol. 54, no. 2, pp. 1185–1195, Feb. 2016.
- [46] R. M. Goldstein, H. A. Zebker, and C. L. Werner, "Satellite radar interferometry: Two-dimensional phase unwrapping," *Radio Sci.*, vol. 23, no. 4, pp. 713–720, Sep. 1988.
- [47] H. Zhang, Y. X. Liu, Y. G. Ji, L. L. Wang, and J. Zhang, "Multi-feature maximum likelihood association with space-borne SAR, HFSWR and AIS," *J. Navigation*, vol. 70, no. 2, pp. 359–378, Oct. 2016.
- [48] R. M. Goldstein, H. Engelhardt, B. Kamb, and R. M. Frolich, "Satellite radar interferometry for monitoring ice sheet motion: Application to an antarctic ice stream," *Science*, vol. 262, no. 5139, pp. 1525–1530, Dec. 1993.



**Zhaoxia Wang** received the B.S. degree in automation and M.S. degree in pattern recognition and intelligent control from the College of Electronic Information Engineering, Inner Mongolia University, Hohhot, China, in 2007 and 2011, respectively. He is currently working toward the doctoral degree in computer applications at the College of Computer Science, Inner Mongolia University, Hohhot, China. His research interests include 3-D imaging radar altimeter image simulation and data processing and satellite networking observation.



**Yongxin Liu** was born in Hohhot, China in 1955. He received the M.S. degree in theoretical physics from Inner Mongolia University, Hohhot, China in 1994 and the Ph.D. degree in control theory and control engineering from Beijing Institute of Technology, Beijing, China, in 2002.

From 2010 to 2011, he was a Visiting Professor with Lund University, Lund, Sweden. He is currently a Professor from the College of Electronic Information Engineering, Inner Mongolia University, Hohhot, China. He is the author of one book and over

120 articles, with research interests including radar detection technology, image processing, information fusion, and intelligent control.



**Chenqing Fan** received the M.S. degree from China University of Petroleum, Qingdao, China, in 2008.

He is currently an Assistant Researcher with the First Institute of Oceanography, Ministry of Natural Resources, Qingdao, China. His research interests include radar altimetry, microwave radar imaging, and ocean remote sensing.



**Jie Zhang** received the Ph.D. degree from Tsinghua University, Beijing, China, in 1993.

He is currently a Researcher with the First Institute of Oceanography, Ministry of Natural Resources, Qingdao, China. His research interests include satellite remote sensing technology, coastal zone high-resolution remote sensing monitoring technology and applications, and marine target monitoring technology.